Desalination and Water Treatment
www.deswater.com
doi: 10.5004/dwt.2021.26453

211 (2021) 1–14
January

Falling film flow characteristics on horizontal tubes and their effects on scale formation in seawater evaporators

Maximilian Waack[a], Heike Glade[a,*], Stephan Nied[b]

[a]*University of Bremen, Engineering Thermodynamics, Badgasteiner Str. 1, 28359 Bremen, Germany, Tel. +49 421 218 64773; emails: heike.glade@uni-bremen.de (H. Glade), maximilian.waack@uni-bremen.de (M. Waack)*
[b]*BASF SE, 67056 Ludwigshafen, Germany, email: stephan.nied@basf.com (S. Nied)*

Received 13 August 2020; Accepted 10 September 2020

ABSTRACT

Horizontal tube falling film evaporators are the main components of multiple-effect distillation plants for seawater desalination. Seawater is distributed onto a horizontal tube bundle and forms a thin film on the outside of the evaporator tubes, which are internally heated by steam. The thickness and the wave motion of the seawater film crucially determine heat and mass transfer rates in the film and, therefore, scale formation on the tube surfaces. Falling film flow on horizontal tubes was studied with a high-resolution optical micrometer in a unique test rig. The liquid film thickness was measured at a high sampling frequency along and around a tube providing information on wave structure and wave frequency at different wetting rates. Moreover, experiments were performed in a horizontal tube falling film evaporator test rig at pilot plant scale with artificial seawater in order to study the formation of calcium- and magnesium-containing salts at different wetting rates. The mean film thickness on the tube surface increases with increasing wetting rate and it highly depends on the position on the tube surface. The wave motion of the film is predominantly governed by liquid impingement at the tube top and liquid detachment at the tube bottom. Scale mass and scale layer thickness are closely connected to falling film characteristics.

Keywords: Falling film; Scale formation; Multiple-effect distillation

1. Introduction

In horizontal tube falling film evaporators, which are commonly used in multiple-effect distillation (MED) plants for seawater desalination, heat transfer and crystallization fouling are massively influenced by film flow characteristics on the evaporator tubes. Seawater is distributed onto the upper tube rows of a horizontal tube bundle by means of spray nozzles. The liquid forms a thin film on the outside of the tubes and trickles down tube by tube. The liquid load can be characterized by the wetting rate Γ which can be defined as the falling film mass flow rate on one side or on both sides of the horizontal tube per unit tube length. In the following, the wetting rate is expressed as the mass flow rate on both sides of the tube per unit tube length:

$$\Gamma = \frac{\dot{m}}{L} \tag{1}$$

The film Reynolds number is a common dimensionless quantity that is used to describe the falling film flow. Different definitions of the film Reynolds number can be found, as described by Mitrovic [1]. In the following, the film Reynolds number is defined as:

$$\mathrm{Re}_F = \frac{2 \cdot \Gamma}{\mu} \tag{2}$$

* Corresponding author.

with the dynamic viscosity μ of the liquid and the wetting rate Γ according to Eq. (1). In falling film evaporators for seawater desalination, the initial wetting rate on the top tube row commonly ranges between 0.06 and 0.14 kg/(s m) [2], which corresponds to a film Reynolds number between 250 and 600 for a seawater temperature of 65°C and a salinity of 35 g/kg. The tubes are heated from the inside by heating steam. As the seawater flows down the tube bundle, it is first preheated and subsequently partly evaporates, decreasing the wetting rate far below the initial values.

Seawater is a multi-component salt solution containing inversely soluble salts, such as calcium carbonate, calcium sulfate and magnesium hydroxide. As the seawater is heated, the solubility of these salts decreases and the supersaturation – the driving force of crystallization – increases. Precipitation of supersaturated salts, mainly calcium carbonate and magnesium hydroxide, preferably starts on the heat transfer surface, forming a scale layer which deteriorates the heat transfer performance. Thus, scale formation needs to be controlled in falling film evaporators to ensure a stable and efficient operation.

Crystallization is driven by supersaturation and it is massively influenced by reaction rates and by mass transfer rates of the involved species towards the heat transfer surface. Mass transfer, in turn, is strongly connected to fluid dynamics. Different flow regimes on and between the horizontal tubes can be identified for different wetting rates.

The intertube flow is characterized by the formation of droplets, jets or sheets on the bottom of each tube [1]. The flow rate, tube spacing, gravity and the physical properties of the liquid determine the flow regime [1]. Droplet formation occurs at low flow rates and large tube spacings. As the flow rate increases or the tube spacing decreases, the flow configuration changes from droplets to jets and finally reaches the sheet regime with interjacent transition regions. Droplets and jets are usually present at common film Reynolds numbers in practical applications. The free surface of the liquid exhibits a wave pattern which can be described by Taylor instability theory [3]. On the tube bottom, droplets/jets detach from locations with maximum wave amplitude [3]. The distance between droplet/jet formation sites decreases with increasing film Reynolds number [4]. In the droplet regime, detachment sites are not simultaneously active at first. With increasing film Reynolds number, more droplets detach at the same time and the droplet frequency increases until continuous jets are formed [5]. In the jet regime with low film Reynolds numbers, jet impingement and detachment sites are inline. As the flow rate increases, two impinging jets form a crest between each other, resulting in a detachment site right underneath [3].

Film flow regimes can generally be described by the physical properties of the liquid, the flow rate and the slope of the substrate [6]. The description is complicated due to the presence of the free surface. Below a critical film Reynolds number, the film is mainly laminar. As the flow rate increases, the free surface is covered with capillary and/or gravity waves, referred to as laminar-wavy regime. Finally, the flow becomes turbulent above a critical film Reynolds number. No matter which flow regime is present, a substantial part of the film is still occupied by a relatively large non-turbulent sublayer [7]. The laminar-wavy regime sets in at a film Reynolds number of 20 for film flow on an inclined plate [8]. The transition of flow regimes on horizontal tubes has rarely been examined. The transition to turbulent flow was reported to occur at a film Reynolds number of 2,000 on a large-diameter horizontal tube [9]. Barba and Di Felice [10] assumed turbulent flow in a horizontal tube falling film evaporator at film Reynolds numbers greater than 1,500. Han and Fletcher [11] postulated a turbulent flow on horizontal tubes in a range of film Reynolds numbers between 770 and 6,800. Parken et al. [12] assumed turbulent flow at film Reynolds numbers above 1,000 for falling film flow on a horizontal tube. Film flow on horizontal tubes is additionally influenced by impinging and detaching droplets/jets. The tube perimeter may be divided into an impingement region and a hydrodynamically fully developed region [13]. The above-mentioned flow regimes are of concern in the fully developed region. Droplet/jet impingement significantly determines heat and mass transfer rates in the impingement region. Moreover, the film is agitated by splashing, inducing surface waves of different nature than capillary and gravity waves.

Several studies of film flow on horizontal tubes have been performed [14–17]. However, the film flow on horizontal tubes has mainly been investigated for the jet regime. Film thickness data are mostly evaluated at circumferential angles between the tube top and the tube bottom. Film flow at circumferential angles of 0° (upper crown line) and 180° (lower crown line) as well as axial variations of film thickness has rarely been examined.

Several methods of measuring the liquid film thickness have been reported in literature [15–17]. Zhang et al. [18] used an optical shadow method, similar to the one in this study, to measure the liquid film thickness on a vertical tube.

The effects of film flow on crystallization fouling in falling film evaporators for seawater desalination have rarely been investigated. Stärk et al. [19] studied scale formation in a falling film evaporator at different wetting rates. Scale layer thickness and scale mass per unit tube surface area decreased with increasing wetting rate. Mabrouk et al. [20] developed a numerical model of a falling film evaporator and showed the effect of an uneven seawater distribution on scale formation.

The objective of this study is to give new insights into the effects of film flow on scale formation in falling film evaporators for seawater desalination.

2. Experimental setup

Experiments were performed in two different test rigs in order to investigate film flow characteristics on horizontal tubes as well as their influence on scale formation.

2.1. Film thickness measurements

In the following, the film thickness test rig and the experimental procedure of the film thickness measurements are described.

2.1.1. Test rig

A unique test rig was constructed for the investigation of the film flow on horizontal tubes, comprising a bank of four

tubes and a high-resolution optical micrometer, as illustrated in Fig. 1.

The test liquid is evenly distributed onto a bank of four horizontal tubes arranged one below the other. A perforated transparent polymer tube with liquid supply at both ends serves as liquid distribution system. The distribution tube has an outer diameter of 16 mm and a wall thickness of 2 mm. Holes with a diameter of 1 mm are aligned with a distance of 5 mm on the bottom of the tube. The center of the distribution tube is positioned 50.5 mm above the center of the first tube. The first two tubes of the test section serve to homogenize the liquid flow. The effective wetted length of the tubes is 300 mm. The vertical distance of the tube centers amounts to 62 mm. Considering a triangular 30° tube pitch in a common tube bundle, this layout represents a realistic tube pitch to diameter ratio of 1.432. The tubes are not heated.

A centrifugal pump conveys the test liquid from a feed tank through a heating coil placed in a thermostat bath to the liquid distribution tube at the top of the test section. The volume flow rate of the test liquid is controlled by a needle valve. Before the test liquid enters the distribution tube, its temperature is measured with a Pt100 temperature sensor (accuracy class A) and its volume flow rate is measured with a turbine flow meter (FCH-midi-PVDF, Biotech, Germany). The flow meter exhibits a measuring accuracy of ±2%.

The liquid film thickness is measured on the third tube by means of a high-resolution optical micrometer (optoCONTROL 2600, Micro-Epsilon, Germany) at a high sampling rate. The micrometer uses LED technology and exhibits a resolution of 0.1 μm, a reproducibility of ±1 μm and a linearity of ±3 μm. The measuring principle is illustrated in Fig. 2. An LED light source produces a parallel light curtain (measuring range 40 mm) which is imaged on a high-resolution CCD camera via a telecentric lens. If an object to be measured is placed in the light curtain, the shadow created by the object will be detected by the CCD camera [21]. The test tube is placed in the light curtain and the shaded length is measured. It is set to zero for the dry tube before each measurement.

Once a liquid film is established, the sensor records the film thickness. The optical micrometer is mounted on a steel frame which, in turn, is directly fixed on the test tube avoiding the measurement of vibrations and thermal expansion. The frame can be moved in axial direction of the tube as well as around the tube. The axial position is measured by means of a potentiometric position sensor (FWA150T, Ahlborn, Germany) with a measuring accuracy of ±0.01 mm. The tilting angle is determined by means of a digital protractor with a measuring accuracy of ±0.1°.

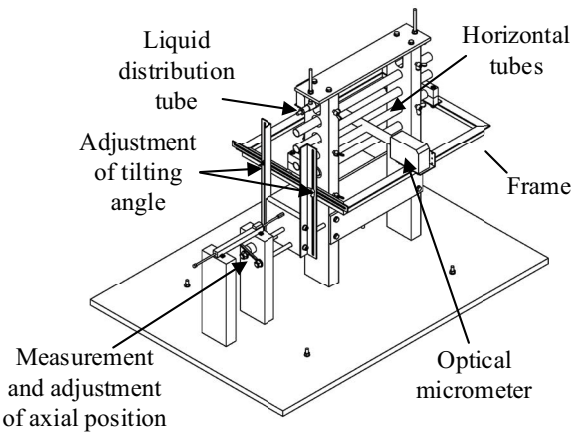

Fig. 1. Film thickness test rig with the high-resolution optical micrometer.

2.1.2. Test procedure

Film flow experiments were performed with deionized water at ambient pressure and a temperature of 25°C, 45°C and 65°C. Aluminum brass tubes (CW 702 R) with an outer diameter of 25.0 mm and a wall thickness of 1.0 mm were used. The tube material as well as the dimensions is widely used in MED plants. The test tubes were thoroughly cleaned with isopropyl alcohol and acetone before each experiment.

The tubes were completely wetted during the measurements of the film thickness. Before each measurement, however, the surface of the third tube (test tube) was locally dried by compressed air and by covering the tube surface directly above the measuring spot along a length of around 3 cm. The film flow above the third tube was not affected by this procedure. The shaded length measured by the LED micrometer was set to zero for the dry tube surface. Afterwards, the blockage of the liquid distribution was removed. The measurement of the film thickness was started once the tube surface was completely rewetted.

As illustrated in Fig. 2, the film thickness was measured on the top and on the bottom of the third tube, referred to as 0° and 180°, respectively, along an axial length of 90 mm. Measurements were performed 45 mm left and right from the center of the wetted tube length at 19 measuring points at a distance of 5 mm whereas the center of the wetted tube length is located at a position of 150 mm. Moreover, the film thickness was measured at circumferential angles between 0° and 180° at three different axial positions, namely the center of the wetted tube length as well as 20 mm left and right from the center. Measurements could only be performed from 0° to 50° as well as from 130° to 140° as the LED light curtain is blocked by the other tubes at high tilting angles of the steel frame and by pendant liquid on the tube bottom at high circumferential angles. Five different wetting rates were applied, as listed in Table 1. In falling film evaporators, wetting rates can easily fall below the initial value

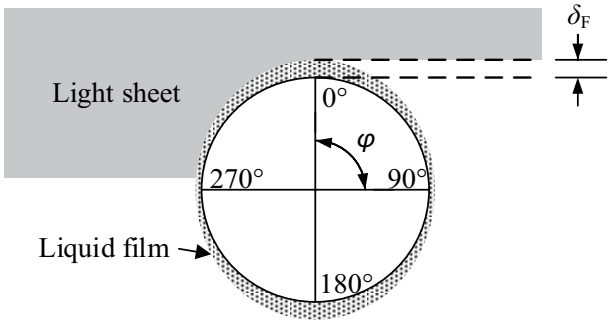

Fig. 2. Measuring principle of the high-resolution optical micrometer.

due to evaporation and liquid maldistributions. Therefore, a minimum value of 0.02 kg/(s m) was chosen. The maximum wetting rate amounted to a common value of 0.10 kg/(s m). At each measuring point, the film thickness was recorded for 5 min at a sampling frequency of 230 Hz.

2.1.3. Test evaluation

Film thickness data were processed in order to determine characteristic film parameters. Owing to the dynamic nature of the liquid film, a wide range of film thicknesses was recorded at each measuring point. Therefore, statistical evaluation of the data was necessary. The mean film thickness and the average minimum film thickness were determined.

The surface of the falling liquid film is in wavy motion. In order to analyze the wave motion, the power spectrum was estimated by means of the Welch's method [22]. The power spectrum was calculated by dividing the data into overlapping segments, computing a modified periodogram for each segment and averaging the periodograms. Segments consist of 600 data points, whereby 400 values are overlapping from segment to segment. In order to increase the resolution in the frequency-domain, zero padding was used and 3,600 additional zeros were added to the end of the time-domain signal. Blackman window was chosen as window function. Peaks in the power spectrum can be attributed to harmonic waves, whereby the peak value represents an estimate of the root mean square value of the amplitude at a specific frequency. The highest peak is related to the maximum amplitude at the dominant frequency. The signal-to-noise ratio was always higher than 50 dB for each measurement.

Table 1
Wetting rates and corresponding film Reynolds numbers for the falling film flow of deionized water at different temperatures applied during the film thickness measurements

Re_F / –		Γ / kg/(s m)				
		0.02	0.04	0.06	0.08	0.10
ϑ / °C	25	44.9	89.9	134.8	179.8	224.7
	45	67.1	134.2	201.3	268.4	335.5
	65	92.3	184.6	277.0	369.3	461.6

2.2. Scaling experiments

In the following, the falling film evaporator test rig and the experimental procedure of the scaling experiments are described.

2.2.1. Test rig

Scaling experiments were performed in a falling film evaporator test rig at pilot plant scale. The main component of the test rig is an evaporator equipped with a bank of six horizontal tubes arranged one below the other, as illustrated in Fig. 3. The tubes are attached to the tube sheets with screws and they are sealed by means of O-rings. The tube length that is wetted by seawater amounts to 453 mm. The vertical distance between the tube centers amounts to 50 mm. Seawater is evenly distributed onto the first tube by a toothed overflow weir and trickles down to the lower tubes, forming a thin film flow. Inspection glasses on both sides of the evaporator shell allow a visual observation of the falling film flow.

The flow diagram of the test rig is illustrated in Fig. 4. The tubes are heated from the inside by heating steam, which is generated by a steam generator. The heating steam condenses inside the tubes and the condensate is directed back to the steam generator. Heat is transferred from the steam inside the tubes to the seawater on the outside of the tubes. The seawater forms a thin film on the outer tube surface. It is first preheated up to saturation temperature on part of the first tube and then partially evaporates on the subsequent tubes. Evaporation takes place at a pressure below ambient pressure, which is maintained by a vacuum pump. The generated vapor is directed to a condenser and the condensate is collected in a tank equipped with a level

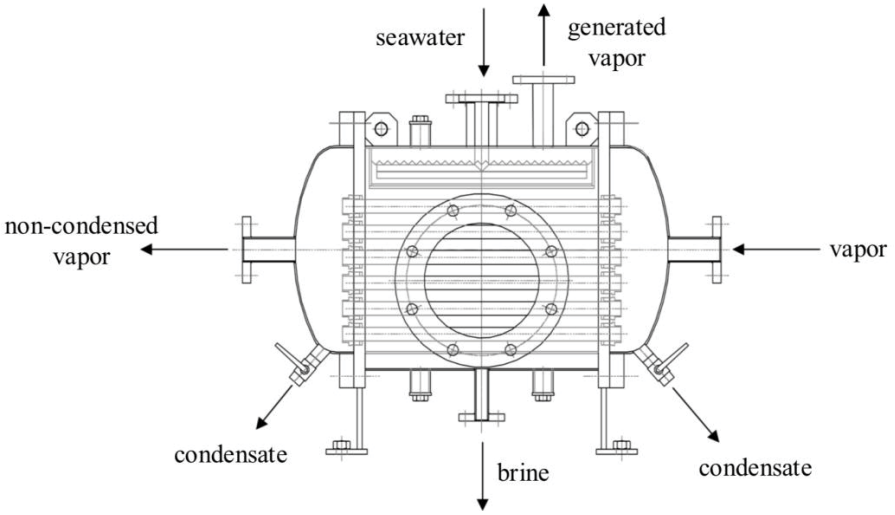

Fig. 3. Drawing of the horizontal tube falling film evaporator [23].

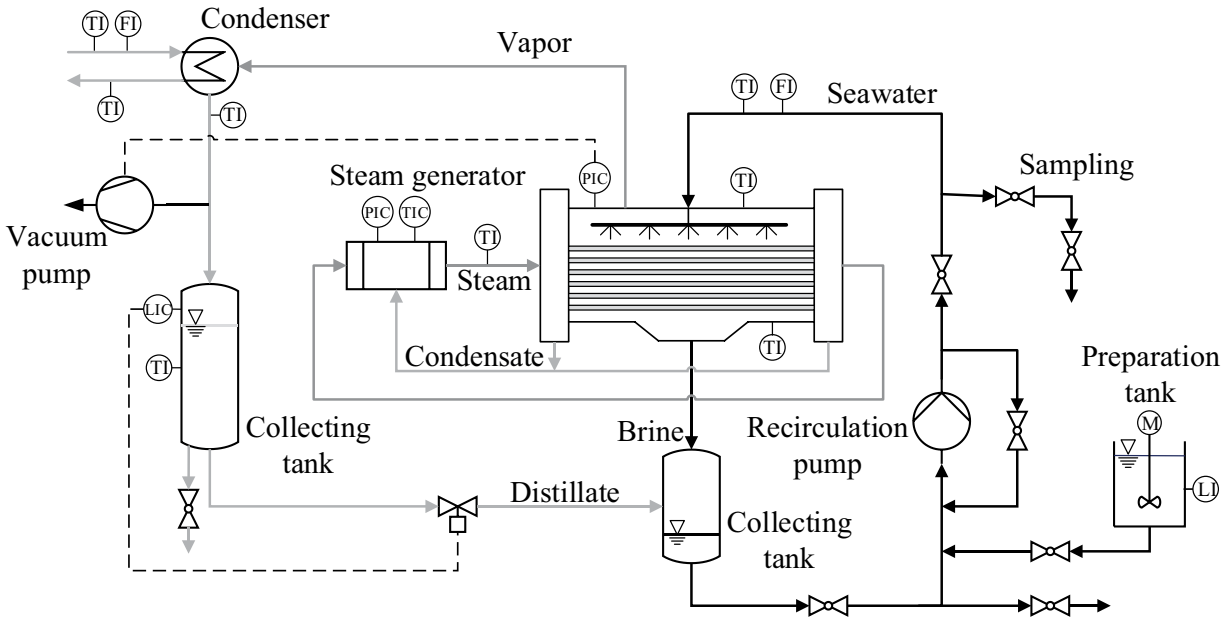

Fig. 4. Flow diagram of the falling film evaporator test rig.

indicator. After leaving the evaporator, the concentrated seawater, referred to as brine, flows into a collecting tank where it is mixed with the distillate in order to keep the salinity of the seawater approximately constant. The seawater is conveyed back to the evaporator by a centrifugal pump.

The test rig is equipped with several temperature, pressure and flow sensors, as illustrated in Fig. 4. Experiments can be carried out at different condensation and evaporation temperatures as well as at different wetting rates.

2.2.2. Test procedure

Experiments were performed with tubes made of aluminum brass, which is an established evaporator tubing material in MED plants. The aluminum brass tubes (CW 702 R) were supplied by MPG Mendener Präzisionsrohr GmbH (Menden, Germany) and had an outer diameter of 25.0 mm and a wall thickness of 1.0 mm. The tubes were used with their typical surface topography as delivered by the tube supplier with a mean surface roughness of 0.73 μm. New tubes were used for each experiment and thoroughly cleaned with deionized water, isopropyl alcohol and acetone.

Artificial seawater with a high salinity of 65 g/kg and an ionic strength of 1.39 mol/kg was used for the scaling experiments, representing concentrated brine at the bottom of an MED tube bundle. The initial pH value was approximately 8.3. The formulation of the artificial seawater originates from oceanography, including 99 mass% of salts in natural seawater [24].

An evaporation temperature of 65°C in the evaporator shell and a condensation temperature of 70°C inside the tubes were chosen, representing common conditions in the first stage of an MED plant. Wetting rates ranging from 0.02 to 0.10 kg/(s m) were applied, as listed in Table 2. Droplet formation is expected at wetting rates below 0.06 kg/(s m) and jet formation at higher wetting rates [25].

Table 2
Wetting rates and corresponding film Reynolds numbers for the scaling experiments with artificial seawater at a temperature of 65°C and a seawater salinity of 65 g/kg

	Γ / kg/(s m)				
	0.02	0.04	0.06	0.08	0.10
Re_F / –	78.5	157.1	235.6	314.1	392.7

Experiments with 240 L of artificial seawater and time periods of 50 h were found to be favorable because time periods are long enough to find differences in scale formation and supersaturation levels are still high enough.

The inside of the evaporator was manually cleaned with deionized water and with diluted acetic acid solution after each test run. The collecting tank for the seawater was cleaned with water jets. The whole circuit was cleaned by flushing with deionized water for several days.

2.2.3. Scale characterization

The scale layers on the tube surfaces were analyzed using different methods. The scale layer thickness was measured by means of a gauge (MiniTest 2100, ElektroPhysik, Germany) in combination with the probe FN 1.6 using the eddy current method. The measuring range of the probe is between 0 and 1,600 μm. It exhibits a high resolution of 0.1 μm. The tolerance amounts to ±1 μm due to the calibration standard. A two-point calibration was performed at each tube. First, the probe was placed on a clean sample determining the lower reference value. Afterwards, a calibration foil with a thickness of 96 μm (±1 μm) was used. The scale layer thickness was measured on each of the six evaporator tubes at four different circumferential angles,

namely 0°, 90°, 180° and 270°. At each circumferential angle, the scale layer thickness was measured at 25 different points along the tube, as shown in Fig. 5. The distance between the measuring points was 20 mm near to the ends of the scale layer and it was 10 mm near to the tube center. The scale layer edges at both tube ends were excluded from the measurements because scale formation is considerably affected by low tube wetting at the tube ends where the tubes are attached to the tube sheets and the scale layer thickness is higher than that on the main tube body. The measurements were repeated 10 times at each position.

Scale formation is dominated by calcium carbonate and magnesium hydroxide precipitation during seawater evaporation [23]. Therefore, the calcium and magnesium contents of the scale on the fourth evaporator tube were determined by inductively coupled plasma atomic emission spectroscopy (ICP-AES). The scale layers at the edges were removed with sandpaper along a length of 1 cm on each side before analysis in order to only determine the scale on the main tube body. The scaled tube was submerged in a 10 mass% acetic acid solution at a temperature of 90°C for 2 h in order to dissolve the scale. The solution was transferred to a beaker and the tube as well as the vessel was extensively rinsed with deionized water which was added to the solution. Afterwards, the solution was boiled down to a volume of about 300 mL. Then the volume was increased to 500 mL by adding deionized water in a volumetric flask. The concentrations of Ca^{2+} and Mg^{2+} ions in the solution were determined with ICP-AES.

3. Results

In the following, the results of the film flow measurements and the scaling experiments are presented.

3.1. Film thickness and wave motion

The intertube flow patterns of deionized water are illustrated in Fig. 6 for different wetting rates ranging from 0.02 to 0.10 kg/(s m) at a temperature of 25°C. At a low wetting rate of 0.02 kg/(s m), only few droplet detachment sites are simultaneously active. The number of active detachment sites increases with increasing wetting rate. The distance of the detachment sites remains approximately constant at each wetting rate. The images only represent an isolated moment. In fact, the detachment sites were not located at a constant position but moved along the bottom of the tube. The flow pattern gradually changes from the droplet regime to the jet regime with increasing wetting rate. The transition seems to occur at a wetting rate of around 0.06 kg/(s m). Whereas the liquid jets almost always fall down vertically at 0.08 kg/(s m), they are more chaotic at 0.10 kg/(s m).

In Fig. 7a, the local mean film thickness is illustrated at the tube top in dependence of the axial position along the tube for different wetting rates at a temperature of 25°C. The local mean film thickness increases with increasing wetting rate. At low wetting rates of 0.02 and 0.04 kg/(s m), the local mean film thickness is almost constant along the tube. Slight variations set in at 0.06 kg/(s m) and major fluctuations occur at 0.08 and 0.10 kg/(s m). Moreover, Fig. 7b shows the impact of different temperatures on the mean film thickness at the tube top based on all 19 measuring points along the upper crown line of the tube. The mean film thickness decreases with increasing temperature at a constant wetting rate.

The local mean film thickness at the tube bottom is illustrated in Fig. 8a in dependence of the axial position along the tube for different wetting rates at a temperature of 25°C. Similarly to the tube top, the local mean film thickness generally increases with increasing wetting rate. There are almost no variations of the local mean film thickness along the tube at low wetting rates. Strong fluctuations along the tube set in at a wetting rate of 0.06 kg/(s m). Generally, the mean film thickness at the tube bottom is about an order of magnitude higher compared with that at the tube top shown in Fig. 7a. The mean film thickness at the tube bottom at various wetting rates for different temperatures is illustrated in Fig. 8b. The mean film thickness at the tube bottom shows no clear dependence on the temperature in the range under examination.

Fig. 9a shows the circumferential variation of the mean film thickness for different wetting rates at a temperature of 25°C. At each circumferential angle, the mean film thickness was determined from data of three different axial positions along the tube, as described in Section 2.1. Analogously to the tube top and tube bottom, the mean film thickness increases with increasing wetting rate on the tube perimeter. At a given wetting rate, the mean film thickness is almost constant on the upper half of the tube at circumferential

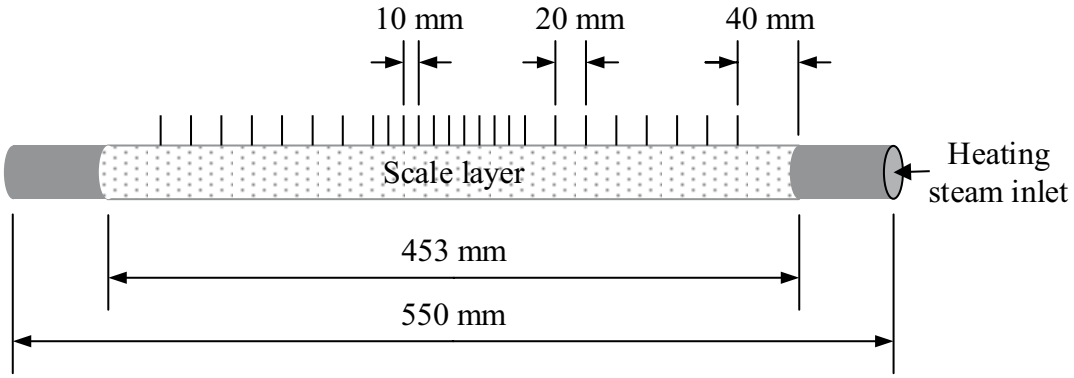

Fig. 5. Positions of the scale layer thickness measuring points on the evaporator tubes.

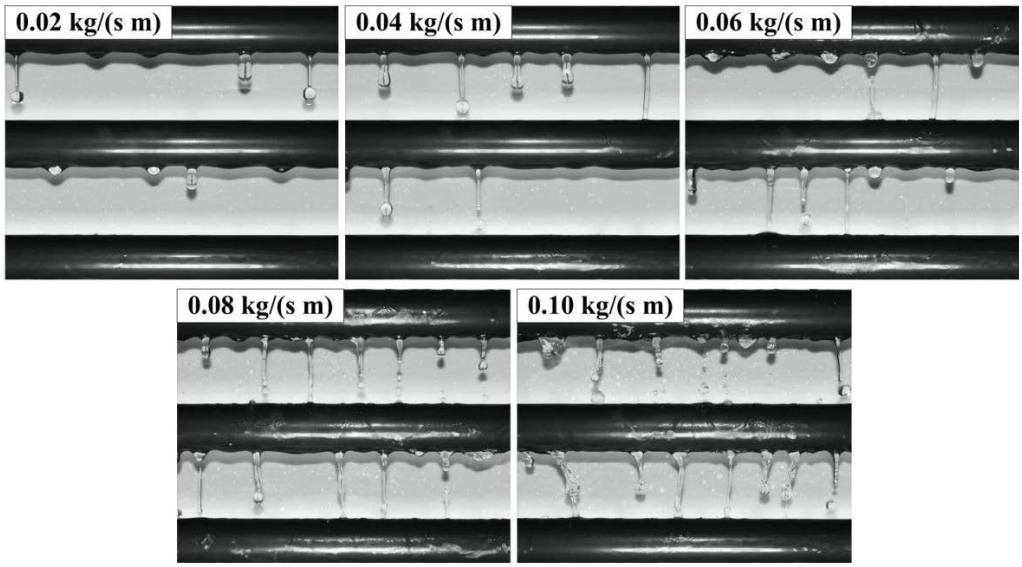

Fig. 6. Intertube flow patterns of deionized water for different wetting rates at a temperature of 25°C.

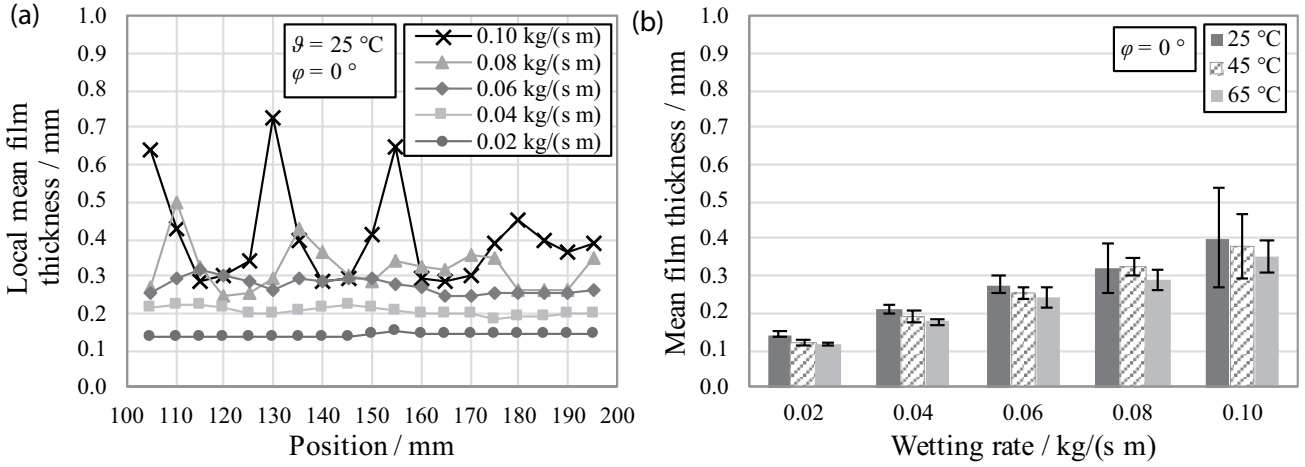

Fig. 7. Local mean film thickness at the tube top (0°) at various axial positions for different wetting rates at 25°C (a) and mean film thickness at the tube top at various wetting rates for different temperatures (b). The local mean film thickness (a) was calculated from data at each measuring point. The mean film thickness (b) was determined from data of all 19 measuring points and the error bars represent the standard mean deviation.

angles above 0° and increases on the lower half of the tube. Local variations of the mean film thickness along the tube increase with increasing wetting rate, which is obvious from the growing size of the error bars, but are negligible for low wetting rates. In Fig. 9b, the mean film thickness is illustrated at various circumferential angles for different temperatures at a wetting rate of 0.04 kg/(s m). The mean film thickness decreases with increasing temperature.

The impact of different wetting rates and temperatures on the average minimum film thickness is illustrated in Fig. 10 for the tube top (a) and for the tube bottom (b). The average values at the tube top and at the tube bottom were determined from measuring data of 19 different axial positions along the upper crown line and along the lower crown line, respectively. In general, the average minimum film thickness decreases with increasing temperature and it is higher at the tube bottom compared with the tube top. At the tube top, a minimum of the average minimum film thickness was detected at a wetting rate of 0.06 kg/(s m). At the tube bottom, the average minimum film thickness increases with increasing wetting rate.

The average minimum film thickness at different circumferential angles and wetting rates is illustrated in Fig. 11. Results are presented for a temperature of 25°C. At each circumferential angle, the average minimum film thickness was determined from measuring data of three different axial positions along the tube. An increasing circumferential angle is accompanied by an increasing minimum film thickness. However, the minimum film thickness shows no clear dependence on the wetting rate.

The wave motion of the liquid film was examined by spectral analysis of the film thickness data. The dominant

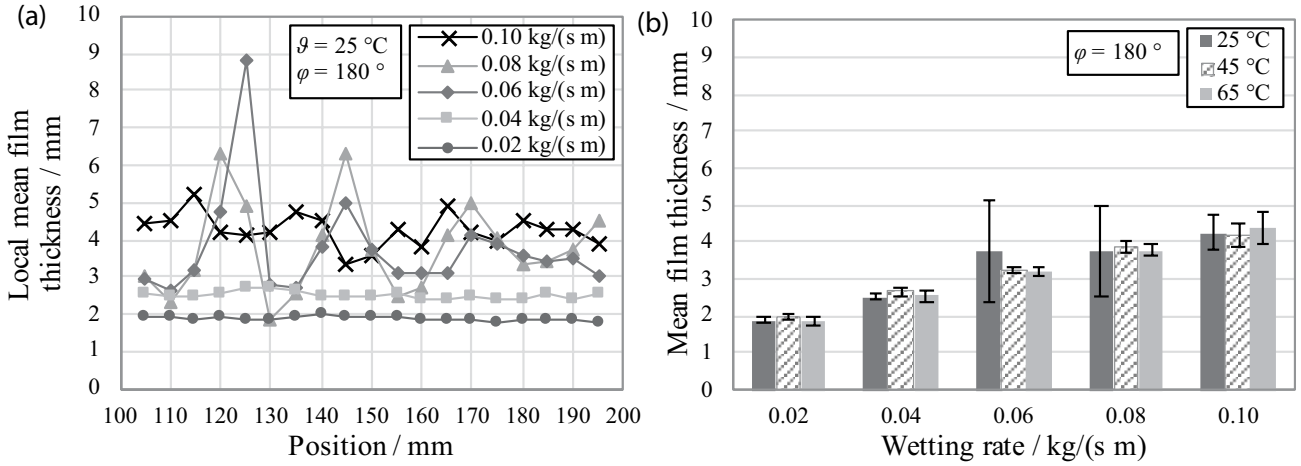

Fig. 8. Local mean film thickness at the tube bottom (180°) at various axial positions for different wetting rates at 25°C (a) and mean film thickness at the tube bottom at various wetting rates for different temperatures (b). The local mean film thickness (a) was calculated from data at each measuring point. The mean film thickness (b) was determined from data of all 19 measuring points and the error bars represent the standard mean deviation.

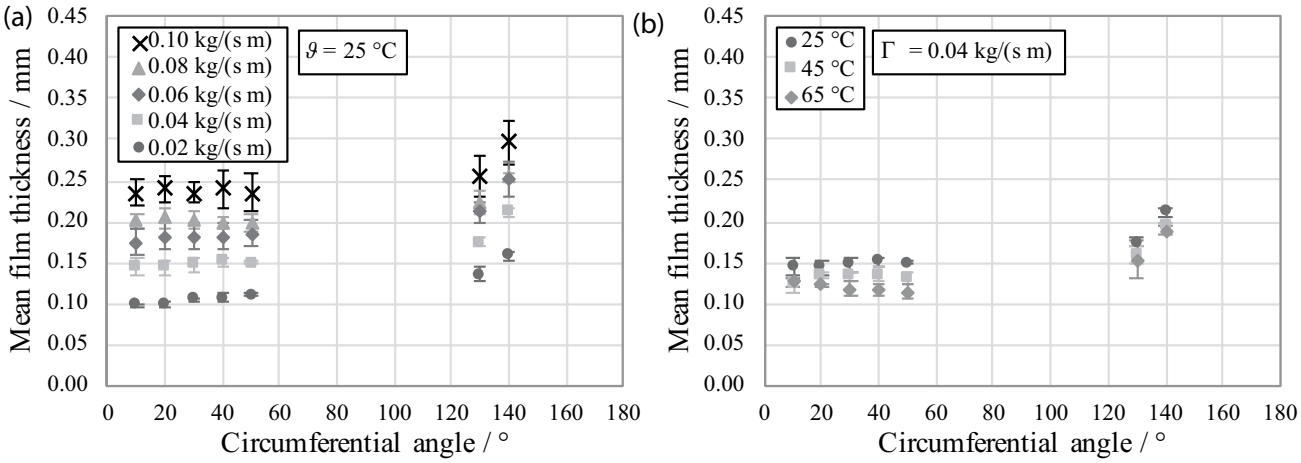

Fig. 9. Mean film thickness at various circumferential angles for different wetting rates at 25°C (a) and mean film thickness at various circumferential angles for different temperatures at a wetting rate of 0.04 kg/(s m) (b). The mean film thickness was determined from data of three different measuring points along the tube. The error bars represent the standard mean deviation.

frequency of the wave motion and its maximum amplitude were determined as characteristic parameters. In the following, results are only presented for a temperature of 25°C. Similar results are obtained for higher temperatures. Neither the maximum wave amplitude nor the dominant wave frequency is substantially affected by changes in temperature. Wave parameters prevailing at the tube top are illustrated in Fig. 12 in dependence of the axial position for different wetting rates at a temperature of 25°C. The dominant frequency increases with increasing wetting rate up to 0.08 kg/(s m) and it is approximately constant along the tube. At a wetting rate of 0.10 kg/(s m), there are positions where the dominant frequency not only further increases but also significantly lower values were detected. The maximum amplitude behaves similarly to the local mean film thickness and increases with increasing wetting rate. There are minor changes of the maximum amplitude along the tube at low wetting rates. At wetting rates of 0.08 and 0.10 kg/(s m), however, the amplitude substantially varies along the tube.

Fig. 13 shows the dominant wave frequency (a) and maximum wave amplitude (b) in dependence of the axial position along the tube at the tube bottom for different wetting rates. In contrast to the tube top, the dominant frequency is independent of the wetting rate and axial position. An almost constant value of around 0.55 Hz was determined. The maximum amplitude at the tube bottom is an order of magnitude higher than that at the tube top, as shown in Fig. 12. The maximum amplitude increases with increasing wetting rate. However, the slope of the increase seems to decline at higher wetting rates. Furthermore, spatial fluctuations of the amplitude are higher for high wetting rates.

Fig. 14 illustrates the characteristic wave parameters in dependence of the circumferential angle for different wetting rates. At a given wetting rate, the dominant frequency

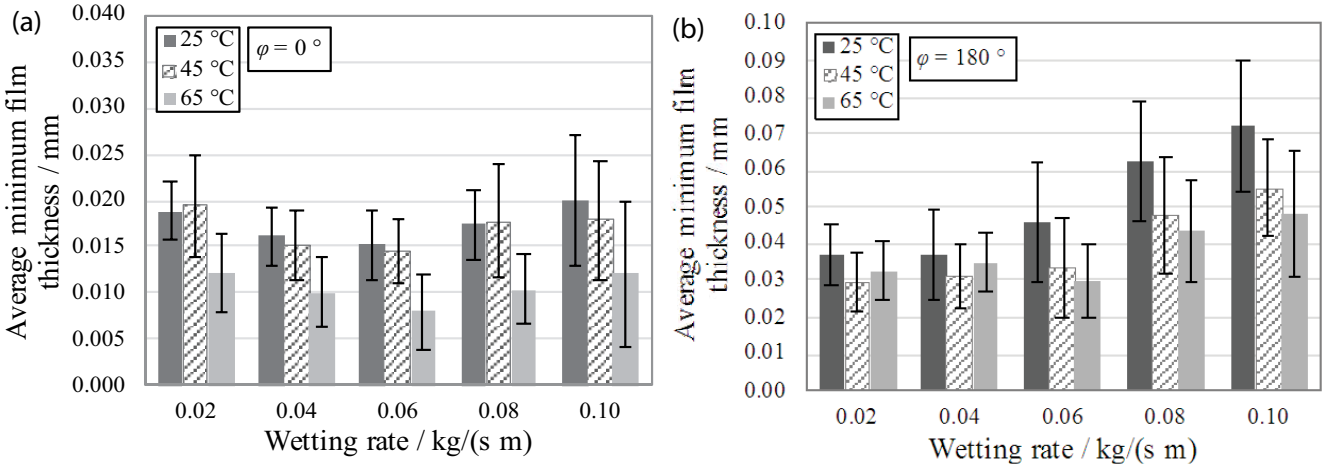

Fig. 10. Average minimum film thickness at the tube top (0°) (a) and at the tube bottom (180°) (b) at different wetting rates. The average values were calculated from data of 19 measuring points along the tube. The error bars represent the standard mean deviation.

remains approximately constant over the perimeter. It increases with increasing wetting rate similarly to the tube top. However, axial variations increase with increasing wetting rate, which is obvious from the growing size of the error bars. The average maximum amplitude exhibits distinct differences in comparison with the mean film thickness. At most circumferential positions, a maximum of the average maximum amplitude was detected at a wetting rate of 0.04 kg/(s m). A further increase of the wetting rate results in a decrease of the maximum amplitude whereas the mean film thickness increases with increasing wetting rate. The amplitude first increases with increasing circumferential angle, then decreases above a circumferential angle of about 30° and eventually increases again on the lower half of the tube.

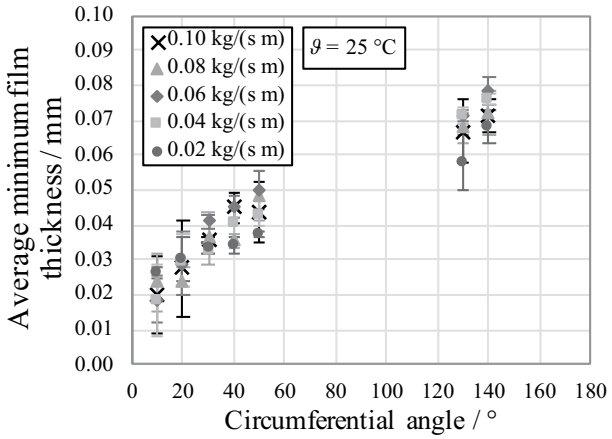

Fig. 11. Average minimum film thickness in dependence of the circumferential angle for different wetting rates at a temperature of 25°C. The average values were determined from data of three different measuring points along the tube. The error bars represent the standard mean deviation.

3.2. Scale formation during seawater evaporation

The calcium and the magnesium scale masses per tube surface area of the fourth evaporator tube are illustrated in Fig. 15 for five different wetting rates ranging from 0.02 to 0.10 kg/(s m). The specific magnesium scale mass is much smaller compared with the calcium scale mass and shows no systematic dependency on the wetting rate. In contrast, the calcium mass is significantly affected by the wetting rate. A lower wetting rate results in a higher calcium mass, whereby the increase of the scale mass with decreasing wetting rate seems to be exponential.

Scale formation is further characterized by the scale layer thickness. The average axial scale layer thickness at different circumferential angles on the fourth test tube is depicted in Fig. 16a. The axial scale layer thickness decreases with increasing wetting rate at each circumferential angle. The thinnest scale layer was detected at the tube bottom followed by the tube top. The thickest scale layer was measured at the tube sides.

Fig. 16b illustrates the average scale layer thickness on each test tube for different wetting rates. The average scale layer thickness increases from the top tube to the bottom tube for each wetting rate. Furthermore, the scale thickness decreases with increasing wetting rate.

4. Discussion

The mean film thickness of a falling water film increases with increasing wetting rate on the whole tube perimeter as a consequence of a higher liquid load. At low wetting rates, the local mean film thicknesses vary only slightly along the tube axis, as shown in Figs. 7 and 8. The liquid detachment sites chaotically move on the tube bottom, which leads to a uniform liquid distribution over time. In contrary, as the intertube flow pattern changes to jet mode, the position of the detachment sites becomes stationary, which is accompanied by peaks of the local mean film thickness along the tube axis at higher wetting rates. The peak values correspond to the most likely positions of the detachment sites.

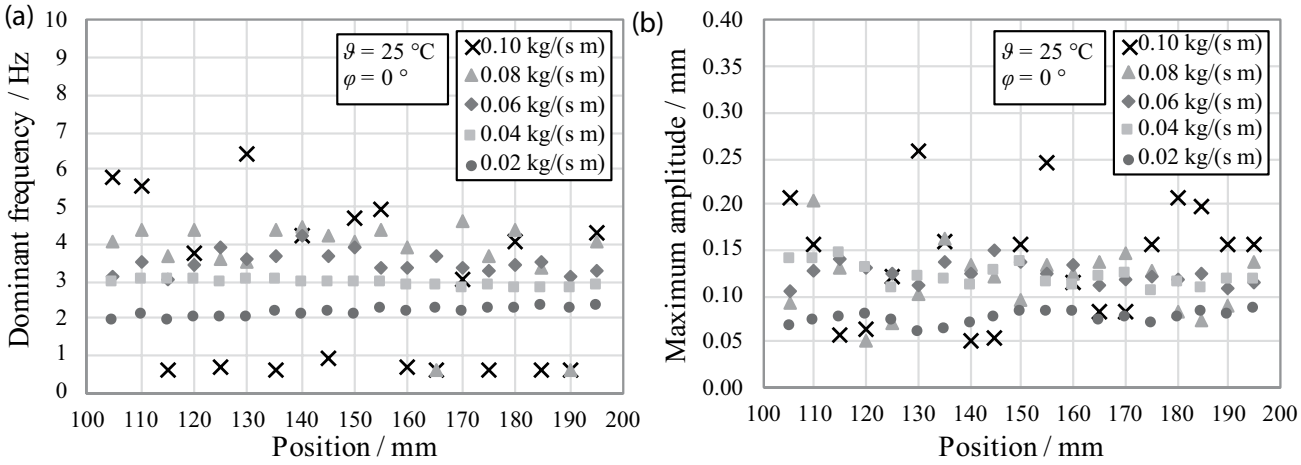

Fig. 12. Dominant wave frequency (a) and maximum wave amplitude (b) at the tube top (0°) in dependence of the axial position for different wetting rates and a temperature of 25°C.

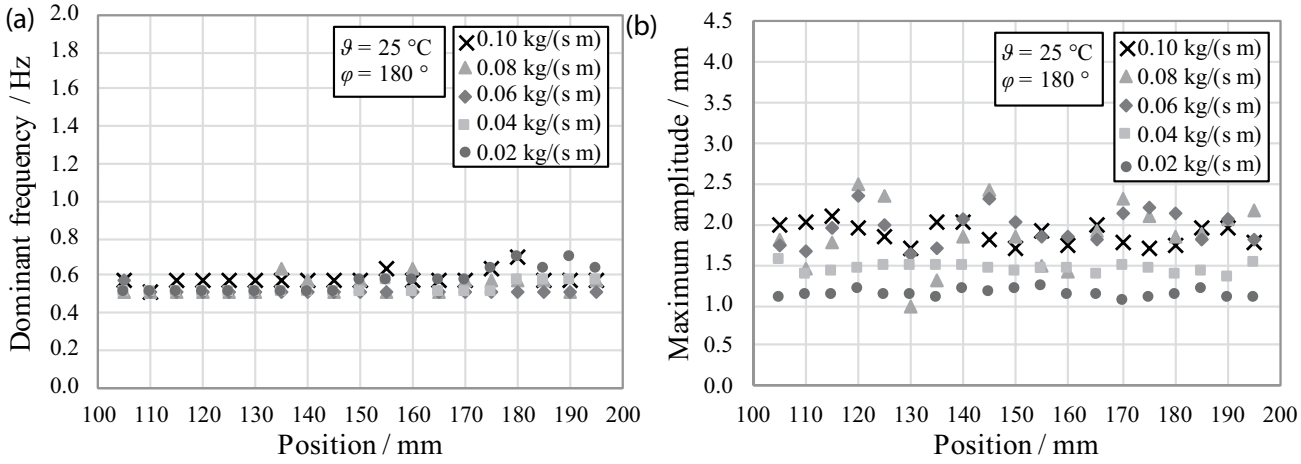

Fig. 13. Dominant wave frequency (a) and maximum wave amplitude (b) at the tube bottom (180°) in dependence of the axial position for different wetting rates at a temperature of 25°C.

The film thickness at the tube bottom is higher compared with that at the tube top because inertia dominates the liquid flow during impingement and capillary effects lead to liquid accumulation on the tube bottom. Figs. 7 and 9 show that the mean film thickness is approximately constant for circumferential angles between 0° and 50° but lower compared with that at the tube top. The liquid is accelerated and, therefore, the film thickness declines. In contrast, the liquid slows down on the lower half of the tube, which results in an increasing film thickness, as shown in Fig. 9. An increasing temperature is accompanied by a decreasing mean film thickness on the upper half of the tube due to a reduced liquid viscosity. Since capillary effects dominate the liquid flow at the tube bottom, no systematic changes of the mean film thickness with temperature can be observed at a circumferential angle of 180°.

Another characteristic parameter of the film flow is the minimum film thickness. As shown in 10a, at the tube top, a minimum of the average minimum film thickness is detected at a wetting rate of 0.06 kg/(s m) for which a transition intertube flow pattern between droplet mode and jet mode prevails. The impingement of a droplet is followed by an inertia dominated spreading process on the surface. As the wetting rate increases, the droplet volume increases for low liquid loads [5]. A higher droplet volume results in a more intensive spreading and, therefore, a lower minimum film thickness. As the intertube flow pattern changes to stable jet mode, a continuous liquid bridge is formed between the tubes. Liquid streams from two neighboring jets interact forming a stagnant crest between each other. Consequently, the axial liquid velocity component is reduced and the minimum film thickness increases. This trend is additionally promoted by the increasing mean film thickness at higher wetting rates, as illustrated in Fig. 8.

While the water flows in tangential direction on the tube surface, energy dissipates and the flow is increasingly dominated by capillary effects. As a result, the minimum film thickness increases with the circumferential angle,

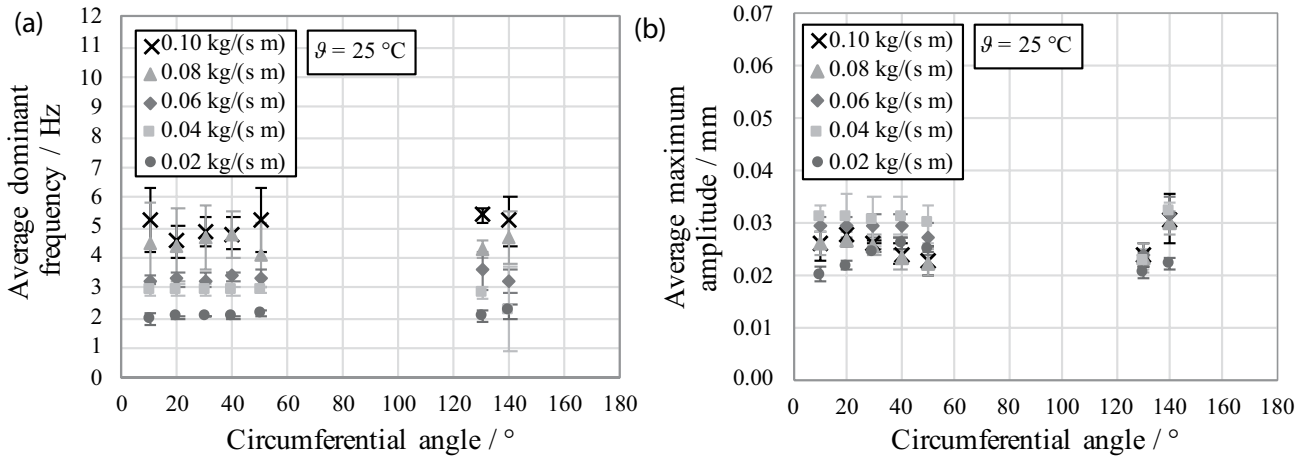

Fig. 14. Average dominant wave frequency (a) and average maximum wave amplitude (b) in dependence of the circumferential angle for different wetting rates at a temperature of 25°C. The average values were determined from measurements at three axial positions. The error bars represent the standard mean deviation.

as depicted in Fig. 11. At the tube bottom, however, the recoiling of detaching liquid bridges as well as the collision of liquid streams induce turbulence so that the average minimum film thickness shown in Fig. 10b is lower compared with that at a circumferential angle of 140°. Moreover, the average minimum thickness increases with increasing wetting rate at the tube bottom, which is attributed to the increasing mean film thickness. Higher temperatures generally reduce the minimum film thickness because viscosity and surface tension are lowered.

Furthermore, the wetting rate crucially affects the wave motion of the water film, characterized by the dominant wave frequency and maximum wave amplitude in this work. As shown in Fig. 12, the dominant wave frequency first increases with increasing wetting rate at the tube top, which reflects the increasing droplet frequency. As a more or less stable jet flow develops at higher wetting rates, the dominant frequency shows strong fluctuations along the tube between 7 Hz and about 0.5 Hz at the tube top. In this case, the dominant frequency correlates with the mean film thickness along the tube. The most likely axial positions of the jet impingement are characterized by peaks of the mean film thickness and the dominant frequency. The wave frequency induced by the droplets also dominates in the range of circumferential angles between 0° and 140°, as shown in Fig. 14. At the tube bottom, however, the same dominant frequency (0.5 Hz) prevails for each wetting rate, shown in Fig. 13. Wave frequencies in this order of magnitude are usually connected to Marangoni instabilities, which derive from surface tension gradients due to temperature gradients [26,27]. Temperature gradients in the film develop in the test rig because no adiabatic conditions prevail and surface perturbations lead to locally varying heat transfer rates in the film. In falling film evaporators, the temperature of the liquid film is nearly constant as soon as the saturation temperature is reached. Therefore, Marangoni instabilities should not play an important role or they are at least less intense during seawater evaporation.

The instability of a falling film on an inclined surface derives from gravity and inertia effects in case of long-wave perturbations [28]. While a liquid film is accelerated, on the one hand, inertia leads to liquid accumulation under the wave crest. On the other hand, the cross-stream component of gravity stabilizes the film due to a higher hydrostatic pressure under the wave crest. However, when the film flows in vertical direction, the cross-stream component of gravity vanishes. Moreover, it changes its direction on the lower half of a horizontal tube leading to an agitation of the surface perturbations. As illustrated in Figs. 12 and 13, the maximum amplitudes at the tube top and the tube bottom rise with increasing wetting rate probably as a consequence of a growing droplet volume and mean film thickness at low wetting rates. Droplet impingement onto the tube top and recoiling of liquid bridges at the tube bottom induce perturbations of the film. The wave amplitude at the tube top grows less with increasing wetting rate at high wetting rates compared with low wetting rates due to the formation of liquid jets between the tubes. While the water flows in tangential direction on the tube surface, the amplitude first increases up to a circumferential angle of about 30°, then decreases and eventually increases again on the lower half of the tube, as shown in Fig. 14. Opposing effects of gravity and inertia presumably lead to the maximum of the maximum amplitude on the upper half of the tube. On the lower half of the tube, the amplitude increases because the cross-stream component of gravity additionally destabilizes the film. The highest maximum amplitude correlates with the highest mean film thickness and prevails at the tube bottom, as shown in Fig. 13.

The effects of film flow on scale formation in falling film evaporators are very complex because heat transfer as well as mass transfer is governed by hydrodynamics. Crystallization depends on the reaction kinetics and the mass transfer of the participating species towards the surface. Moreover, deposited salt crystals can be removed by shear forces.

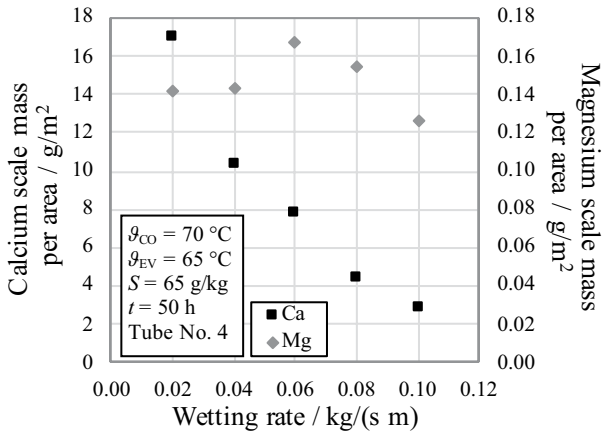

Fig. 15. Deposited calcium and magnesium mass per tube surface area for different wetting rates on the 4th tube.

The falling film flow on the horizontal tubes was non-turbulent in the experimental range of film Reynolds numbers, as listed in Table 1, comparing with critical film Reynolds numbers from literature [9–12]. Kocamustafaogullari and Chen [29] assumed that the flow on a horizontal tube can be approximated by the flow on inclined surfaces. According to this assumption and the transition criteria formulated by Ishigai and Nakanisi [30] for the flow pattern on an inclined plate, the falling film on the horizontal tubes was in laminar-wavy motion in the experimental range of film Reynolds numbers. Although the film surface exhibits a wave pattern in the laminar-wavy mode, a relatively thick laminar sublayer is present [7]. As a result, the heat transfer on the tube surface is promoted by a decreasing liquid film thickness in the investigated range of film Reynolds numbers. The same trend holds for the mass transfer assuming an analogy between heat and mass transfer, as widely suggested [31–34]. The highest transport coefficients are expected at the tube top since droplet or jet impingement agitates the film and the thermal boundary layer is not yet fully developed [35]. In turn, the slowest transport processes are presumably present at the tube bottom in the investigated range of film Reynolds numbers [35].

Scale formation in falling film evaporators for seawater desalination is reported to be dominated by calcium carbonate precipitation, which can be confirmed by experimental results [23,36,37]. The deposited calcium scale mass per surface area is significantly higher compared with the magnesium scale mass at each wetting rate. Former analysis of scale from the same falling film evaporator test rig with X-ray diffraction has shown that calcium carbonate primarily precipitates in the form of aragonite [37].

Calcium carbonate crystallization can be either diffusion-controlled or reaction-controlled [38–43]. In case of a reaction-controlled calcium carbonate precipitation, the temperature is expected to have the greatest impact on the fouling process [42]. Film flow massively influences heat transfer and, consequently, the temperature profile along and around the evaporator tube. Moreover, the saturation limits of salts are significantly determined by the substrate surface temperature. A higher temperature results in a higher supersaturation of the inversely soluble salts. Since the heat transfer coefficients in the evaporating laminar falling film are higher at lower wetting rates, the outer tube wall temperature decreases with decreasing wetting rate and scale formation might be reduced. However, scale formation was most severe at low wetting rates. Consequently, calcium carbonate precipitation is most probably controlled by mass transport in falling film evaporators in the range of wetting rates from 0.02 to 0.10 kg/(s m) at an evaporation temperature of 65°C and a driving temperature difference of 5 K. Further discussion will be based on the assumption that scale formation is diffusion-controlled.

Film flow characteristics can be used to explain changes in scale formation. The liquid temperature is nearly constant in falling film evaporators as soon as the saturation temperature is reached. Therefore, Marangoni instabilities should not play an important role or they are at least less intense. However, it should be noted that the temperature-induced Marangoni effect may affect the film flow in the film thickness test rig. Moreover, the film thickness measurements were performed with deionized water, while seawater was used in the scaling experiments. Dissolved salts showed no effect on the film thickness in experiments performed by Hou et al. [16], while a scale layer decreased the film thickness. Chen et al. [17] reported a slight increase of the film thickness with seawater compared with pure water. Hence, film flow characteristics in the falling film evaporator test rig might slightly differ from those measured in the film thickness test rig. However, the scale characteristics measured in the falling film evaporator test rig correlate well with the film flow characteristics measured in the film thickness test rig.

As shown in Fig. 15, the calcium scale mass per surface area is massively reduced when the wetting rate is increased, which confirms the results of Stärk et al. [19]. In contrast, the magnesium scale mass, which is already relatively low, shows no obvious dependency on the wetting rate. Calcium carbonate crystallization on the heat transfer surface is increased by lower wetting rates due to higher mass transfer rates. In contrast, magnesium hydroxide precipitation is unaffected by hydrodynamics and rather determined by electrochemical effects [37,44]. This trend is confirmed by the scale layer thickness measurements for different wetting rates, as shown in Fig. 16. The scale layer thickness is the lowest at the highest wetting rate.

The strongest scale formation occurred at the sides of the tubes (90° and 270°) followed by the tube top. Least scale formed on the tube bottom, as depicted in Fig. 16. Film thickness measurements revealed that the mean film thickness as well as the average minimum film thickness is smaller at the tube top compared with the tube bottom, as illustrated in Figs. 7 and 8. Thinner films lead to a smaller mass transfer resistance at the tube top promoting scale formation. Additionally, impinging droplets and jets agitate the film. Dominant wave frequencies are high and maximum amplitudes are about half of the size of the mean film thickness further intensifying mass transfer. Moreover, thinner films result in higher heat transfer coefficients and, therefore, high evaporation rates. As a consequence, the smaller minimum film thickness at the top of the tubes leads to high local supersaturations increasing salt precipitation. On the

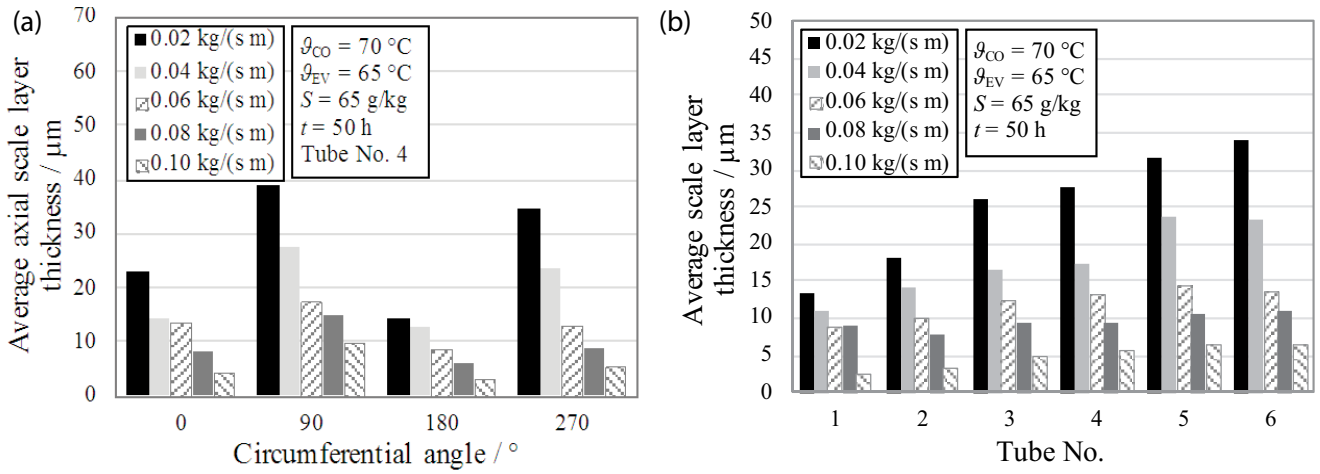

Fig. 16. Average axial scale layer thickness at different circumferential angles on the 4th test tube (a) and average scale layer thickness on each test tube (b), both illustrated at different wetting rates.

bottom of the tubes, films are thick and the dominant wave motion exhibits a low frequency. Therefore, scale formation is less severe at the tube bottom.

The mean film thickness is smaller at the tube sides compared with that at the top and bottom. However, transfer rates are expected to be the highest at the tube top due to droplet or jet impingement, which simultaneously increases shear forces leading to higher scale removal rates. Since the strongest scale formation was determined at 90° and 270°, the effect of higher removal rates seems to be dominant at the tube top.

Furthermore, scale formation generally increases from the top tube to the bottom tube, as shown in Fig. 16. Seawater evaporates, which is accompanied by an increasing salt concentration, and therefore higher supersaturations promote scale formation.

5. Conclusions

Falling film flow plays an important role in scale formation on the heat exchanger tubes in horizontal tube falling film evaporators for seawater desalination. Heat and mass transfer are influenced by film thickness and wave motion of the thin seawater film on the tubes. In order to extend the knowledge of film flow on horizontal tubes and to give new insights into the impact of falling film characteristics on scale formation, extensive investigations of film flow and scale formation were performed under various wetting conditions.

Liquid film thicknesses on the bottom of the tube exceed thicknesses on the top by an order of magnitude. The thinnest film is formed on the tube sides. The mean film thickness increases with increasing wetting rate. Wave formation on the tube top is dominated by droplet/jet impingement, whereas capillary effects govern the film flow at the tube bottom.

Least scale is formed at the bottom of the tube. The scale formation on the top is stronger than that at the bottom. The scale thickness is highest at the tube sides. This trend correlates very well with the film thickness measurements. The deposited calcium mass per tube surface area and the scale layer thickness increase with decreasing wetting rate. Assuming diffusion-controlled calcium carbonate crystallization in the laminar-wavy falling film, increasing scale formation can be explained by an intensified mass transfer due to thinner liquid films and wave motion.

In future work, film thickness measurements will be performed under the influence of different surface-active substances in order to evaluate their effect on film flow and scale formation.

Acknowledgments

The authors would like to thank BASF SE (Ludwigshafen, Germany) and Solenis Technologies Germany GmbH (Krefeld, Germany) for supporting the scale analysis.

Symbols

L	—	Tube length, m
$\dot{m}$	—	Liquid mass flow rate on both sides of the tube, kg/s
Re_F	—	Film Reynolds number, –
S	—	Salinity, g/kg
t	—	Time, h
x	—	Axial position, mm
Γ	—	Wetting rate, kg/(s m)
δ_F	—	Liquid film thickness, mm
ϑ	—	Temperature, °C
μ	—	Dynamic viscosity, Pa·s
ϕ	—	Circumferential angle, °

References

[1] J. Mitrovic, Flow structures of a liquid film falling on horizontal tubes, Chem. Eng. Technol., 28 (2005) 684–694.
[2] H. Glade, S. Cetinkaya, S. Will, S. Nied, G. Schürmann, Effects of the wetting rate on scale formation in multiple-effect distillers, Proc. EuroMed, Dead Sea, Jordan, 2008.
[3] X. Hu, The Intertube Falling-Film Modes: Transition, Hysteresis, and Effects on Heat Transfer, PhD Thesis, University of Illinois, 1995.

[4] X. Hu, A.M. Jacobi, Departure-site spacing for liquid droplets and jets falling between horizontal circular tubes, Exp. Thermal Fluid Sci., 16 (1998) 322–331.
[5] D. Maron-Moalem, S. Sideman, A.E. Dukler, Dripping characteristics in a horizontal tube film evaporator, Desalination, 27 (1978) 117–127.
[6] G.D. Fulford, The flow of liquids in thin films, Adv. Chem. Eng., 5 (1964) 151–236.
[7] L.K. Brumfield, T.G. Theoanous, On the prediction of heat transfer across turbulent liquid films, J. Heat Transf., 98 (1976) 496–502.
[8] R.B. Bird, W.E. Stewart, E.N. Lightfoot, Transport Phenomena, John Wiley & Sons, Inc., New York, 2002.
[9] J.T. Rogers, S.S. Goindi, Experimental laminar falling film heat transfer coefficients on a large diameter horizontal tube, Can. J. Chem. Eng., 67 (1989) 560–568.
[10] D. Barba, R. Di Felice, Heat transfer in turbulent flow on a horizontal tube falling film evaporator - a theoretical approach, Desalination, 51 (1984) 325–333.
[11] J.C. Han, L.S. Fletcher, Falling film evaporation and boiling in circumferential and axial grooves on horizontal tubes, Ind. Eng. Chem. Process Design Dev., 24 (1985) 570–575.
[12] W.H. Parken, L.S. Fletcher, V. Sernas, J.C. Han, Heat transfer through falling film evaporation and boiling on horizontal tubes, J. Heat Transf., 112 (1990) 744–750.
[13] M.-C. Chyu, A.E. Bergles, An analytical and experimental study of falling-film evaporation on a horizontal tube, J. Heat Transf., 109 (1987) 983–990.
[14] J.D. Killion, S. Garimella, Gravity-driven flow of liquid films and droplets in horizontal tube banks, Int. J. Refrig., 26 (2003) 516–526.
[15] X. Wang, M. He, H. Fan, Y. Zhang, Measurement of falling film thickness around a horizontal tube using laser-induced fluorescence technique, J. Phys. Conf. Ser, 147 (2009), doi: 10.1088/1742–6596/147/1/012039.
[16] H. Hou, Q. Bi, H. Ma, G. Wu, Distribution characteristics of falling film thickness around a horizontal tube, Desalination, 285 (2012) 393–398.
[17] X.D. Chen, S. Shen, Y. Wang, J. Chen, J. Zhang, Measurement on falling film thickness distribution around horizontal tube with laser-induced fluorescence technology, Int. J. Heat Mass Transf., 89 (2015) 707–713.
[18] J.T. Zhang, B.X. Wang, X.F. Peng, Falling liquid film thickness measurement by an optical-electronic method, Rev. Sci. Instrum., 71 (2000) 1883–1886.
[19] A. Stärk, K. Loisel, K. Odiot, A. Feßenbecker, A. Kempter, S. Nied, H. Glade, Wetting behaviour of different tube materials and its influence on scale formation in multiple-effect distillers, Desal. Water Treat., 55 (2015) 2502–2514.
[20] A.A. Mabrouk, K. Bourouni, H.K. Abdulrahim, M. Darwish, A.O. Sharif, Impact of tube bundle arrangement and feed flow pattern on the scale formation in large capacity MED desalination plants, Desalination, 357 (2015) 275–285.
[21] Micro-Epsilon Messtechnik GmbH & Co. KG, optoControl 2600 - High resolution LED micrometer, Technical information sheet. Available at: www.micro-epsilon.co.uk (accessed June 5, 2020).
[22] P.D. Welch, The use of fast Fourier transform for the estimation of power spectra: a method based on time averaging over short, modified periodograms, IEEE Trans. Audio Electroacoust., 15 (1967) 70–73.
[23] C. Wildebrand, Zum Einsatz polymerer Additive zur Reduktion der Belagbildung in Horizontalrohr-Verdampfern für die Meerwasserentsalzung, PhD Thesis, University of Bremen, 2006.
[24] D.R. Kester, I.W. Duedall, D.N. Connors, R.M. Pytkowicz, Preparation of artificial seawater, Limnol. Oceanogr., 12 (1967) 176–179.
[25] J. Mitrovic, Wärmeübergang in Rieselfilmen an waagrechten Rohren, VDI Verlag, Düsseldorf, 1990.
[26] M. Sumiji, S. Nakamura, K. Onuma, T. Hibiya, Optical measurement of resonant oscillation and Marangoni convection-induced oscillation in a molten silicon surface, Japan. J. Appl. Phys., 39 (2000) 3688–3693.
[27] H. Linde, M.G. Velarde, A. Wierschem, W. Waldhelm, K. Loeschcke, A.Y. Rednikov, Interfacial wave motions due to Marangoni instability. I. Traveling periodic wave trains in square and annular containers, J. Colloid Interface Sci., 188 (1997) 16–26.
[28] S. Kalliadasis, C. Ruyer-Quil, B. Scheid, M.G. Velarde, Falling Liquid Films, Springer, London, 2012.
[29] G. Kocamustafaogullari, L.Y. Chen, Falling film heat transfer analysis on a bank of horizontal tube evaporator, AIChE J., 34 (1988) 1539–1549.
[30] S. Ishigai, Z. Nakanisi, Hydrodynamics and heat transfer of vertical falling liquid films, Bull. JSME, 15 (1972) 594–602.
[31] T.H. Chilton, A.P. Colburn, Mass transfer (absorption) coefficients - prediction from data on heat transfer and fluid friction, Ind. Eng. Chem., 26 (1934) 1183–1187.
[32] W. Ambrosini, N. Forgione, A. Manfredini, F. Oriolo, On various forms of the heat and mass transfer analogy: discussion and application to condensation experiments, Nucl. Eng. Design, 236 (2006) 1013–1027.
[33] J.H. Lienhard IV, J.H. Lienhard V, A Heat Transfer Textbook, Phlogiston Press, Cambridge, 2006.
[34] J.G. Collier, J.R. Thome, Convective Boiling and Condensation, Oxford University Press, New York, USA, 1994.
[35] K.P. Hupe, Wärmeübertragung am berieselten horizontalen Rohr, Chemie Ingenieur Technik, 34 (1962) 609–614.
[36] C. Wildebrand, H. Glade, S. Will, M. Essig, J. Rieger, K.-H. Büchner, G. Brodt, Effects of process parameters and anti-scalants on scale formation in horizontal tube falling film evaporators, Desalination, 204 (2007) 448–463.
[37] K. Krömer, S. Will, K. Loisel, S. Nied, J. Detering, A. Kempter, H. Glade, Scale formation and mitigation of mixed salts in horizontal tube falling film evaporators for seawater desalination, Heat Transf. Eng., 36 (2015) 750–762.
[38] A. Helalizadeh, H. Müller-Steinhagen, M. Jamialahmadi, Mixed salt crystallisation fouling, Chem. Eng. Process., 39 (2000) 29–43.
[39] N. Spanos, P.G. Koutsoukos, Kinetics of precipitation of calcium carbonate in alkaline pH at constant supersaturation. Spontaneous and seeded growth, J. Phys. Chem. B, 102 (1998) 6679–6684.
[40] J.W. Morse, R.S. Arvidson, A. Luttge, Calcium carbonate formation and dissolution, Chem. Rev., 107 (2007) 342–381.
[41] X.K. Xing, C.F. Ma, Y.C. Chen, Mechanism of calcium carbonate scale deposition under subcooled flow boiling conditions, Chin. J. Chem. Eng., 13 (2005) 464–470.
[42] T.M. Pääkkönen, M. Riihimäki, C.J. Simonson, E. Muurinen, R.L. Keiski, Crystallization fouling of $CaCO_3$ - analysis of experimental thermal resistance and its uncertainty, Int. J. Heat Mass Transf., 55 (2012) 6927–6937.
[43] N. Andritsos, M. Kontopoulou, A.J. Karabelas, P.G. Koutsoukos, Calcium carbonate deposit formation under isothermal conditions, Can. J. Chem. Eng., 74 (1996) 911–919.
[44] M.K.V. Nair, B.M. Misra, Electrolytic scale formation in sea water distillation systems, Desalination, 25 (1978) 263–268.